



Novel donor-acceptor-acceptor ternary conjugated microporous polymers with boosting forward charge separation and suppressing backward charge recombination for photocatalytic reduction of uranium (VI)

Fengtao Yu^{a,b}, Zhiqiang Zhu^b, Shiping Wang^b, Jinyu Wang^a, Zhenzhen Xu^a, Fangru Song^b, Zhimin Dong^b, Zhibin Zhang^{b,*}

^a Jiangxi Key Laboratory for Mass Spectrometry and Instrumentation, East China University of Technology, Nanchang 330013, PR China

^b State Key Laboratory of Nuclear Resources and Environment, East China University of Technology, Nanchang 330013, PR China

ARTICLE INFO

Keywords:

Photoreduction uranium
Donor-acceptor-acceptor
Conjugated microporous polymers
Forward charge transfer
Backward charge recombination

ABSTRACT

The photoreduction of soluble U(VI) to insoluble U(IV) with conjugated microporous polymers (CMPs) is a promising channel to remove uranium from radioactive wastewater efficiently. However, the rapid backward charge recombination and unsatisfactory forward charge transfer lead to undesirable photocatalytic activity of CMPs. Herein, for the first time, a series of D-A₁-A₂ terpolymers is developed with statistical copolymerization through adjusting the monomer feed molar ratio (FMR) for photoreduction of uranium. Compared with D-A binary copolymer, such D-A₁-A₂ terpolymers can inhibit charge recombination and simultaneously facilitate charge separation due to its larger dipole moment and giant built-in electric field. Therefore, the PTrSO-2 which the FMR is 0.75: 1.0: 0.75 achieves 99.5% photocatalytic U(VI) reduction efficiency within 120 min visible-light irradiation, outshining most reported photocatalysts for such applications. This work cultivates an emerging stratagem and unconventional thinking for the development of CMPs photocatalysts used in the effective treatment of radioactive wastewater.

1. Introduction

Nuclear energy (or atomic energy) is the energy released from the nucleus through nuclear reactions, which has the advantages of cleanliness, efficiency and economy. Considered to be the most promising candidate to replace traditional fossil energy on a large scale [1,2]. As a "strong nuclear cornerstone, nuclear power granary", uranium resources play an important supporting role in the nuclear fuel cycle system [3]. Uranium is the element with the largest atomic number (92) in nature and has both radioactivity and chemical toxicity. In the process of vigorously developing the nuclear industry, a large amount of uranium-containing radioactive wastewater will be inevitably discharged, which poses a huge threat to the environment [4]. Thus, how to safely treat U(VI) from wastewater is still a hot topic.

Recently, reducing the highly soluble and environmentally mobile hexavalent uranium (UO₂²⁺) to sparingly soluble and relatively immobile tetravalent uranium (such as UO₂) has emerged as an attractive strategy for removing uranium from the contaminated water due to its highly efficiency, eco-friendly and low cost [5,6]. Indeed, U(VI) can be

reduced to U(IV) through biologically [7–9], chemically [10,11], and photocatalytic technology [12,13]. Regrettably, on the one hand, the active ingredients in microorganisms and chemically reducing materials used to reduce uranium are easily oxidized and deactivated in the air. On the other hand, poor recyclability severely limits the development of these two types of methods. Comparatively, sunlight light-driven semiconductor photocatalytic reduction technology is highlighted due to its highly efficiency, no secondary pollution, reusability and low energy input. Over the past few decades, the rapid development of photocatalytic technology has witnessed the contribution of inorganic semiconductor photocatalysts (such as TiO₂ [14–16], TiO₂/Fe₃O₄ [17], SrTiO₃/Ti₃C₂ [18], Ti₃C₂/CdS [19], MOFs [20] and so on) in the field of photocatalytic reduction of uranium. Nevertheless, the weak visible light absorption and difficult-to-adjust the photoelectrochemical performance have become the key factors that limit the photocatalytic activity of inorganic semiconductors.

For decades, as another class of photoactive semiconductor, organic polymers have gained much attention owing to their structural diversity, strong visible-light absorption and adjustable electronic structure [21].

* Corresponding author.

E-mail address: zhbzhang@ecut.edu.cn (Z. Zhang).

<https://doi.org/10.1016/j.apcatb.2021.120819>

Received 8 August 2021; Received in revised form 24 September 2021; Accepted 11 October 2021

Available online 14 October 2021

0926-3373/© 2021 Elsevier B.V. All rights reserved.

Inspired by graphite carbon nitride (g-C₃N₄) [22–26], many types of new organic polymers, such as conjugated polymers (CPs) [27,28], conjugated microporous polymers (CMPs) [29–31], covalent triazine-based frameworks (CTFs) [32,33], covalent organic frameworks (COFs) [34,35], porous aromatic framework (PAFs) [36–38] and polymer dots [39,40], have been intensively researched as the photocatalyst. Among them, the donor-acceptor (D-A) type CMPs display relatively satisfactory photocatalytic activity because D and A possess significantly different electron affinity and then induce generation of a large dipole moment, resulting in the formation of a stronger built-in electric field (Fig. 1b). Excited by light, photo-generated electron-hole pairs are immediately generated, and then the electrons are rapidly transferred from D to A under the drive of the built-in electric field, thereby achieving effective separation of electrons and holes [41–45]. For instance, our group took the lead in synthesizing the dibenzothiophene dioxide-containing D-A type CMP (ECUT-SO), which showed excellent photocatalytic reduction of uranium activity due to the efficient separation of light-induced e^-/h^+ pairs [46]. Subsequently, the sulfonic acid-containing D-A type CMP (PyB-SO₃H) has been obtained by us via the post-sulfonation strategy, which also exhibits high-efficiency photocatalytic reduction of U(VI) activity [47]. However, the π -conjugated systems are prone to swift backward charge recombination at the same time, leading to limited photocatalytic activity. To achieve more effective photocatalytic U(VI) reduction by CMPs, the key challenge is to develop effective strategies to suppress backward charge recombination and simultaneously promote forward charge transfer. Inspired by the photosynthesis system II in nature (Fig. 1a), constructing system with multiple electron-rich (donors) or electron-poor (acceptors) units with clear energy level gradients may be an effective method to inhibit the backward charge recombination and promote photo-generated carrier separation [48,49].

To this end, a series of D-A₁-A₂ CMPs (Fig. 1c and Scheme 1), in which the 3,9-dibromoperylene (M1) serves as D, the 2,4,6-tris(4-(4,4,5,5-tetramethyl-1,3,2-dioxaborolan-2-yl)phenyl)-1,3,5-triazine (M2) and 3,7-dibromodibenzothiophene-S,S-dioxide (M3) act as the primary electron acceptor (A₁) and the secondary (A₂) electron acceptors, respectively, have been successfully synthesized with the Suzuki–Miyaura polymerization reaction. Hereafter, the obtained CMPs serve as photo-induced electron-transfer photocatalyst to achieve efficient photocatalytic reduction of U(VI). Moreover, a statistical copolymerization strategy has been taken to tune optimize CMPs band gap (E_g) to gain the "Goldilocks Zone" [50], in which the E_g is narrow enough to

obtain a better visible light capture and the conduction band (CB) is negative enough to enable U(VI) reduction, and where molecular dipole is sufficiently large to promote intramolecular charge transfer and prevent the undesired backward charge recombination. It is found that the high dependence of CMPs photocatalytic activity upon the feed molar ratio (abbreviated as FMR) of M1, M2 and M3 (M1: M2: M3). As a result, the PTrSO-2 terpolymer with the FMR of 0.75: 1.0: 0.75 has the optimal E_g of 2.00 eV, efficient charge separation and suppressed charge recombination, achieving 99.5% photocatalytic U(VI) reduction efficiency within 120 min, which outperforms the state-of-the-art organic polymers and even comparable to some high-performance inorganic semiconductor materials (Table S1). The present results prove that the D-A-A CMPs has a bright prospect for purifying radioactive wastewater.

2. Experimental section

2.1. Materials and characterization

2,4,6-tris(4-bromophenyl)-1,3,5-triazine, dibenzo[b,d]thiophene 5,5-dioxide, bis(pinacolato)diboron, Pd(dppf)Cl₂, [Pd(dppf)]Cl₂ x DCM, Pd(PPh₃)₄, potassium acetate, N-Bromosuccinimide (NBS), uranyl nitrate (UO₂(NO₃)₂·6H₂O), azo arsenic III, chloroacetic acid, sodium acetate, tertiary butanol (TBA), p-benzoquinone (p-BQ), potassium bromate (KBrO₃), methanol and 5,5-Dimethyl-1-pyrroline-N-oxide (DMPO) are obtained from Alfa Aesar Ltd. TBA, p-BQ, KBrO₃ and methanol are used to scavenge hydroxyl radicals (\bullet OH), superoxide radicals ($O_2^{\bullet-}$), electron (e^-) and hole (h^+), respectively. The monomer of 3,9-dibromoperylene is obtained from Jilin Chinese Academy of Sciences-Yanshen Technology Co., Ltd. Notably, all chemicals are used as received and without further purification unless otherwise noted. The detailed characterizations of the prepared samples are shown in Supporting Information (ESI).

2.2. Preparation of CMPs

The target CMPs are synthesized by referring to the Suzuki–Miyaura cross-coupling polycondensation method used in our previous study [46,47]. Briefly, the monomers (M1, M2, M3 or M4) and Pd(PPh₃)₄ are added in a 100 mL Shrek tube. The mixture is degassed by freeze-pump-thaw technique for over three times and sealed under vacuum. Then, DMF (30.0 mL) and K₂CO₃ solution (2.0 M, 5.0 mL) are injected into the above mixture. The resulting solution is heated to

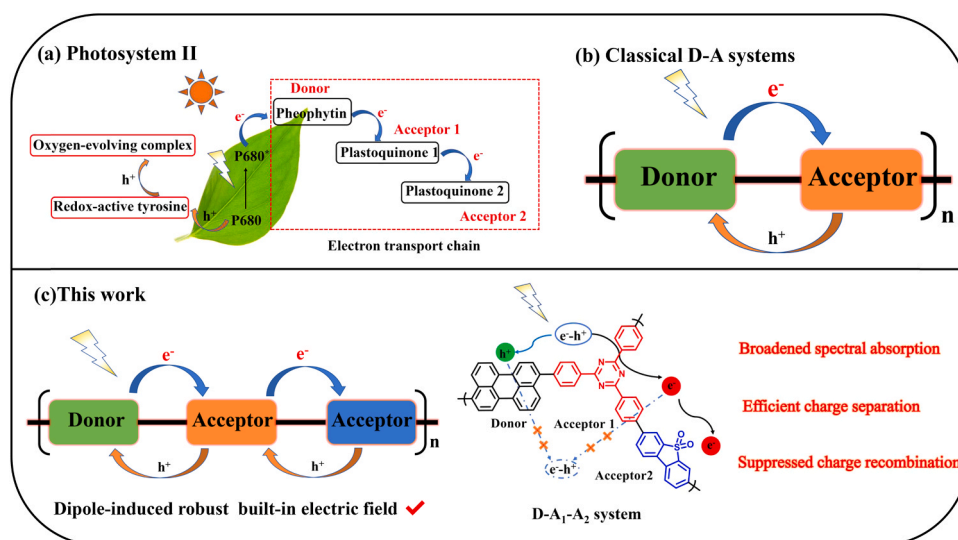
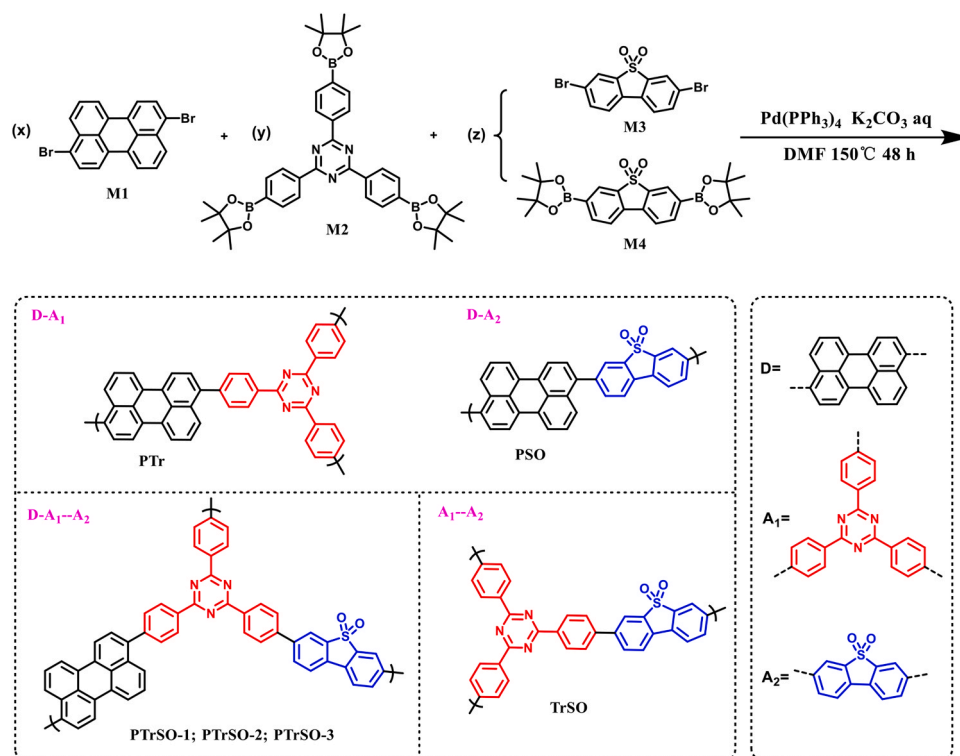


Fig. 1. (a) Electron transfer path in photosystem II after photo-excitation of P680; (b) Classical D-A systems exhibiting simple electron-hole separation; (c) D-A₁-A₂ system in the photoinduced electron-transfer process in this work.



Scheme 1. The synthetic pathway toward D-A₁-A₂ containing copolymer CMPs photocatalysts by statistical copolymerization strategy.

150 °C and stirred for 48 h. Subsequently, the mixture solution is cooled to RT and filtrated. The obtained filter cake is further purified by Soxhlet extraction technology successively with methanol, acetone, chloroform and tetrahydrofuran (100.0 mL for each) for 48 h, respectively, until the extracts solution becomes colorless. The resulting polymers are dried in a vacuum at 80 °C overnight and obtained the product. The detailed synthesis process is shown in [Supporting information \(ESI\)](#).

2.3. Photocatalytic reduction of uranium (VI)

All photocatalytic experiments are conducted in a jacketed quartz beaker photoreactor cooled by circulating water (Instrument Model: CEL-APR250H). Typically, 50.0 mg as-prepared CMPs is added into 100.0 mL 50.0 ppm U(VI) solutions (containing 10.0 mL methanol), followed by 2 min ultrasonication and stirring continuously. Subsequently, the solution pH value is adjusted using a negligible volume of NaOH (0.1 M) or HNO₃ (0.1 M) solutions. Before irradiation, the resulting mixture is continuously stirred in the dark for 60 min to achieve adsorption-desorption equilibrium. Then, the suspension is illuminated with a 300 W Xe lamp (Light source model: SHX-F300) with a 400 nm cut-off filter. At given times, aliquot (2.0 mL) of the solution is pipetted and filtered through 0.22 μm Nylon syringe filters. The concentration of U(VI) in the supernatant solution is determined by spectrophotometric method, which arsenazo-III is selected as the chromogenic agent and the corresponding maximum absorption wavelength is set to 652 nm. The blank test for comparison, which is implemented under the same conditions as above except that no photocatalyst is added. Furthermore, the influences of pH, initial U(VI) concentration and coexisting interference ions on the photocatalytic U(VI) reduction performance are also investigated. In the experiment of exploring active species, TBA, *p*-BQ, KBrO₃ and CH₃OH scavengers are added to neutralize •OH radicals, •O₂⁻ radicals, electrons and holes, respectively.

2.4. DFT calculation methods

Density functional theory (DFT) calculations are performed using the

Gaussian 16 program package. All structures and the frontier molecular orbitals are optimized without symmetry constraints at the CAM-B3LYP/6-311 G(d, P) level [51,52].

3. Results and discussion

3.1. Molecular design and synthesis

To further promote the Frenkel excitons separation efficiency of D-A conjugated polymers and suppress the recombination of electron-hole pairs, a series of D-A₁-A₂ ternary CMPs with large dipole moment is innovatively proposed. As shown in [Scheme 1](#), the target D-A₁-A₂ CMPs are synthesized through the statistical copolymerization strategy, which can systematically control the polymer structure and adjust the dipole moment via different monomer FMR [53,54]. The FMR is variable to tune the electronic structure of CMPs to obtain the D-A₁-A₂ system for optimal photocatalytic U(VI) reduction activity. The obtained D-A₁-A₂ CPMs are marked as PTrSO-1, PTrSO-2 and PTrSO-3, which corresponding monomer FMR are 1.0: 1.0: 0.5, 0.75: 1.0: 0.75 and 0.5: 1.0: 1.0, respectively. In addition, the PTr (D-A₁), PSO (D-A₂) and TrSO (A₁-A₂) for comparison are obtained by copolymerizing two monomers separately. As far as we know, the CMPs are firstly reported here except for TrSO, which is previously researched for hydrogen evolution (named as Triazine-Ph-CPP) [45]. All co-polymerizations reactions are carried out with the classic Pd(0)-catalyzed Suzuki-Miyaura polycondensation and the corresponding synthesis process are elaborated in the ESI section.

3.2. Morphological and structural characterization

All of the obtained CMPs are insoluble, chemically stable and amorphous solid powders ([Fig. S1a](#)), which is consistent with most literature reports [29–31]. Thermogravimetric analysis (TGA, [Fig. S1b](#)) curves certificate all the obtained CMPs possess perfectly thermal stability, and the disintegration temperature is about 500 °C in N₂ atmosphere. The surface morphologies of the D-A₁-A₂ CMPs are observed

using SEM. As displayed in Fig. 2, the PTrSO-1, PTrSO-2 and PTrSO-3 have a similar nanoparticle morphology. Moreover, from the TEM images (Fig. 2), a large number of nanopores can be observed in D-A₁-A₂ CMPs, but the samples show amorphous texture, which is consistent with the corresponding amorphous structure (Fig. S1a).

In addition, their chemical structure is specifically characterized with the FT-IR spectroscopy, solid-state ¹³C NMR spectra, elemental analysis and XPS spectroscopy. Seen from the FT-IR spectroscopy (Figs. S2 and 3a), the obvious skeleton vibration peaks at 1608 and 1573 cm⁻¹ belong to the aromatic ring of all CMPs. Notably, the peaks near 1505 and 1357 cm⁻¹ are the C=N and the C-N stretching vibration of the triazine ring from triazinyl-containing CMPs (PTrSO-1, PTrSO-2, PTrSO-3, TrSO and PTr) and their triazine breathing mode can be seen as a sharp signal around 810 cm⁻¹. Predictably, the two strong signals around 1300 and 1156 cm⁻¹ of sulfone-containing CMPs (PTrSO-1, PTrSO-2, PTrSO-3, TrSO and PSO) are the symmetric and asymmetric vibration peaks of sulphonyl group, respectively. The solid-state ¹³C NMR spectra (Fig. 3b) further verify the terpolymers (PTrSO-1, PTrSO-2 and PTrSO-3) are successfully obtained according to simultaneously existing the characteristic chemical shifts of carbon in the triazine ring (N-C=N $\delta \approx 168.0$ ppm) and the typical signal of the carbon bonding to the sulfone (CSO₂, $\delta \approx 140.0$ ppm).

Furthermore, X-ray photoelectron spectroscopy (XPS) analyses are carried out to extremely investigate the composition and the surface chemical states of the obtained CMPs (Figs. S3 and 3c-e). As shown in the XPS survey spectra (Fig. 3c), the main chemical components of PTrSO-1, PTrSO-2, and PTrSO-3 are carbon (C), nitrogen (N), oxygen (O) and sulfur (S), identifying the coexistence of perylene, triazinyl and sulfone groups. The S species in sulfone-containing CMPs are found around at 169.00 and 167.80 eV which can be assigned to the S2p_{1/2} and S2p_{3/2} in sulphonyl groups, respectively (Fig. 3d). In addition, the high-resolution N 1s spectra of triazinyl-containing CMPs are shown in Fig. 3e. The binding energy of the sp²-hybridized aromatic nitrogen of D-A₁-A₂ CMPs (398.52, 398.58 and 398.66 eV for PTrSO-1, PTrSO-2 and PTrSO-3, respectively) lies between that of PTr (398.48 eV) and TrSO (398.78 eV). The difference is caused by the introduction a certain amount of sulfone group with stronger electron-withdrawing ability than triazinyl into the backbone, which provides strong evidence for the successful preparation of terpolymers.

3.3. Specific surface area and pore size distribution

Nitrogen adsorption/desorption curves (Figs. 3f, S4 and Table 1) revealed that all the CMPs are porous with the microporous nature, evidenced by the steep rise of nitrogen adsorption isotherm curves at low relative pressures and the similar pore size distribution with the micropore diameter at ca. 1.0 nm. The Brunauer–Emmett–Teller (BET) surface area of PTr, PTrSO-1, PTrSO-2 and PTrSO-3 are 429, 445, 505 and 219 m² g⁻¹, respectively. Known from the test results, the specific surface area increases with increasing the dibenzothiophene-S, S-dioxide (SO) content from PTr to PTrSO-2. However, for PTrSO-3, further increasing the SO, the corresponding specific surface area decreases. The difference in BET of CMPs may be due to the different monomer structures and variable comonomer ratios. The M2 with three polymerizable sites usually forms a 3D cross-linked polymer network structure, while the bi-functionalized M1 and M3 (or M4) will produce a linear polymer structure, which is not conducive to the formation of pores. Therefore, the polymers with large specific surface area which is conducive to a high photocatalytic activity can be conveniently obtained by changing the feed ratio of comonomers (Table 2).

3.4. Optical performance and energy band structure

Conventionally, the visible-light capture properties of all the CMPs are further investigated with UV/vis absorption diffuse reflectance spectra (DRS). The energy gaps (E_g) of CMPs are calculated according to Tauc-plot, and the corresponding lowest unoccupied molecular orbital (LUMO) values are estimated with Mott–Schottky plots. Seen from the DRS (Fig. 4a), all the as-obtained CMPs display a broad visible-light absorption range from 400 to 800 nm. Compared with traditional D-A polymers, D-A₁-A₂ terpolymers which have stronger intramolecular charge transfer (ICT) from D to A₁ to A₂ show a wider visible light response range and darker apparent color (Fig. S5). Interestingly, as the SO content increases, the D-A₁-A₂ type CMPs first show a bathochromic-shift of absorption spectrum, followed by a hypochromic-shift. The M-S plots (Fig. S6) of the copolymers reveal that the LUMO energy values shift to the less negative and the HOMO energy values shift to more positive with the amount of SO unit increased, and they all have enough driving force to trigger the reduction reaction of UO₂²⁺ to UO₂. Therefore, introducing the SO unit can regulate the E_g of the terpolymers to a certain extent (from 2.00 to 2.14 eV) (Fig. 4b and c). More importantly,

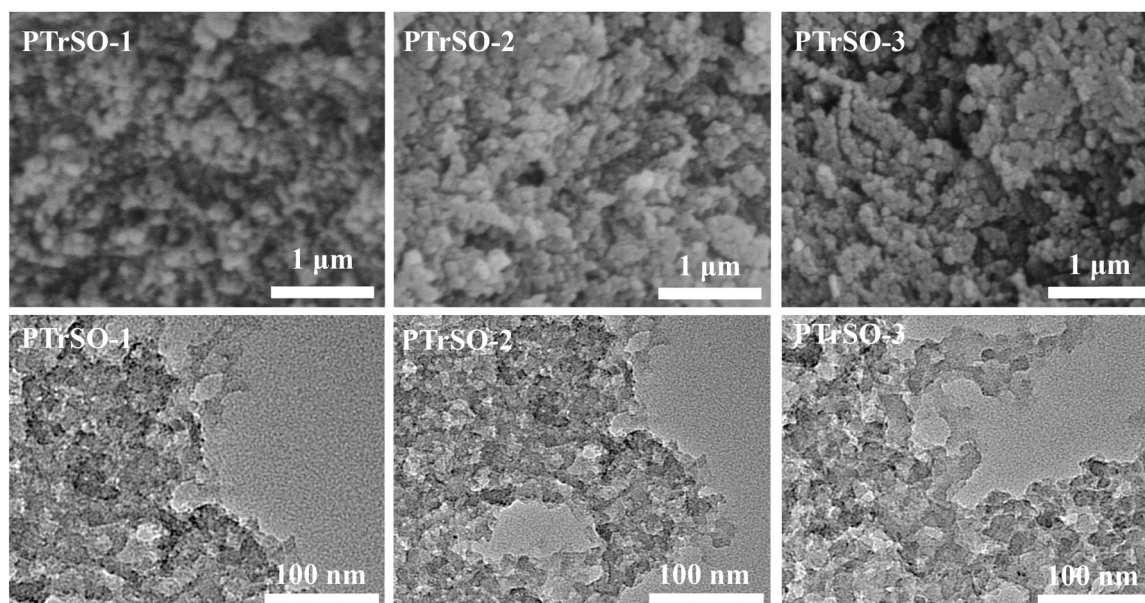


Fig. 2. The three pictures above show the SEM of PTrSO-1, PTrSO-2 and PTrSO-3; The three pictures below show the TEM of PTrSO-1, PTrSO-2 and PTrSO-3.

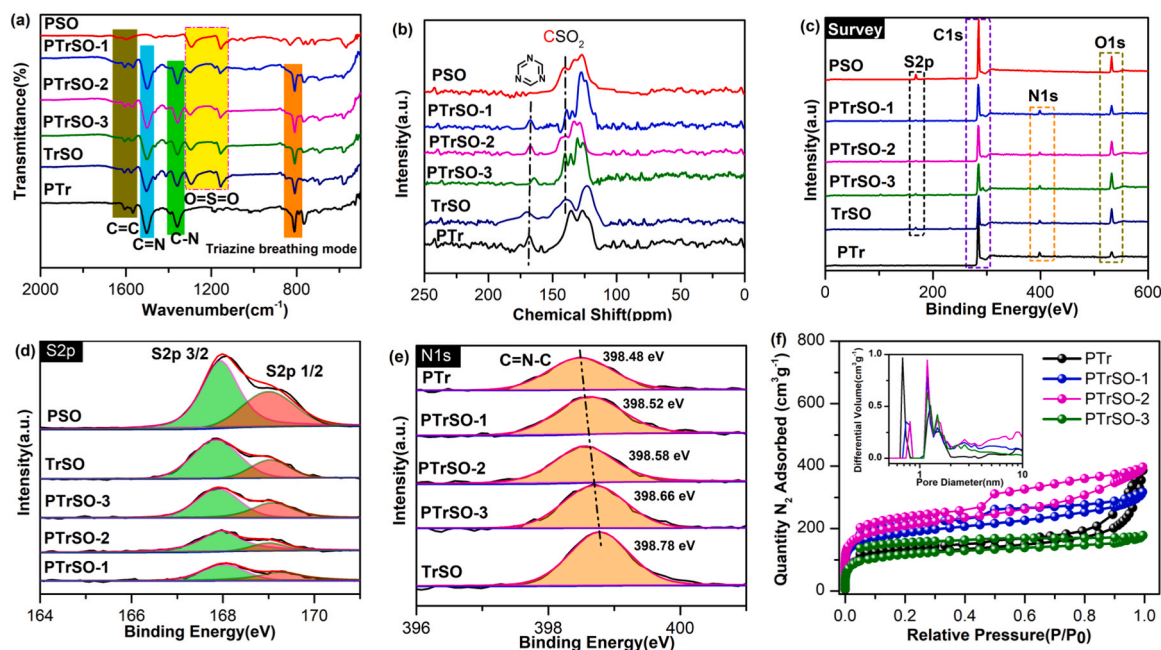


Fig. 3. (a) The FT-IR spectra of the obtained CMPs; (b) The solid-state ^{13}C NMR spectra of obtained CMPs; (c) XPS survey spectra; (d) High-resolution XPS spectra of S2p; (e) High-resolution XPS spectra of N1s; (f) Nitrogen adsorption/desorption curves at 77 K and the corresponding pore size distribution curves of PTr, PTrSO-1, PTrSO-2 and PTrSO-3 via NLDTF calculation (inset).

Table 1

Monomer feed ratio and surface area of the copolymers.

| Polymers | Monomer molar ratio | | | | $S_{\text{BET}}^{[a]}/\text{m}^2\text{g}^{-1}$ |
|----------|---------------------|-----|------|-----|--|
| | M1 | M2 | M3 | M4 | |
| PTr | 1.5 | 1.0 | 0 | 0 | 429 |
| PSO | 1.0 | 0 | 0 | 1.0 | 39 |
| PTrSO-1 | 1.0 | 1.0 | 0.5 | 0 | 445 |
| PTrSO-2 | 0.75 | 1.0 | 0.75 | 0 | 505 |
| PTrSO-3 | 0.5 | 1.0 | 1.0 | 0 | 219 |
| TrSO | 0 | 1.0 | 1.5 | 0 | 198 |

[a] The surface area is calculated from N₂ adsorption isotherm.

among all the obtained CMPs, the terpolymer PTrSO-2 has the narrowest E_g of 2.00 eV and widest visible light response range. Generally, a wider light absorption range indicates a longer π -conjugated chain, which achieve better electron delocalization, which is beneficial for the photocatalytic reaction.

3.5. Electron transfer dynamics

A series of photo-electrochemical tests are implemented to monitor

Table 2

Photophysical property and Photocatalytic reduction efficiency of uranium for the CMPs photocatalysts.

| Polymers | $\lambda_{\text{em}}^{[a]}$ (nm) | HOMO ^[b] /V | $E_g^{[c]}$ /eV | LUMO ^[d] /V | Removal ^[e] (%) | $k^{[f]}$ /min ⁻¹ |
|----------|----------------------------------|------------------------|-----------------|------------------------|----------------------------|------------------------------|
| PTr | 560 | +1.03 | 2.14 | -1.11 | 85.3 | 0.016 |
| PSO | 586 | +1.29 | 2.06 | -0.77 | 95.5 | 0.026 |
| PTrSO-1 | 595 | +1.12 | 2.04 | -0.92 | 98.6 | 0.035 |
| PTrSO-2 | 599 | +1.11 | 2.00 | -0.89 | 99.5 | 0.044 |
| PTrSO-3 | 603 | +1.17 | 2.02 | -0.85 | 98.9 | 0.038 |
| TrSO | 450 | +2.18 | 2.81 | -0.63 | 71.6 | 0.011 |

[a] Photoluminescent emission peak of the CMPs recorded in the solid state;

[b] The HOMO energy level calculated from optical gap and M-S;

[c] The E_g calculated by Tauc-Plot;

[d] The LUMO energy level measured by MS;

[e] The photocatalytic U(VI) reduction efficiency is obtained within 120 min visible light irradiation;

[f] The reduction rates constant (k) at 293.15 K are obtained according to the pseudo first-order kinetics model ($\ln(c_0/ct) = kt$).

the inhibition of backward charge recombination and the promotion of forward charge transfer/separation behavior, as crucial factors affecting the photocatalytic activity of organic polymer semiconductors. The steady-state photoluminescence (PL) spectroscopy which comes from the recombination of photogenerated electrons and holes is a valid measure to characterize the backward charge recombination rate. As shown in Fig. 5a, the CMPs obtained by changing the FMR show different emission peaks and intensities. In contrast to PTr, PSO and TrSO, the fluorescence emission peaks is red-shifted and the corresponding PL intensity is distinctly quenched after constructing D-A₁-A₂ structure, owing to the extended π -conjugate structure and significant energy level gradient which suppresses the electron-hole recombination. Very significantly, the PTrSO-2 exhibits a distinctly red-shifted emission at approximately 605 nm with much lower PL intensity than that of other CMPs, which suggests that the recombination of the electrons and holes are effectively suppressed. Additionally, the charge separation and transfer process are directly detected by contact potential difference (CPD) measurement. Usually, the value of CPD is used to measure the concentration of photogenerated holes. Fig. 5b displays the steady state CPD images of as-obtained CMPs in the dark and illumination at 500 nm. Very interestingly, all the samples obtain an increase in CPD under illumination, indicating photogenerated holes quickly migrated to the

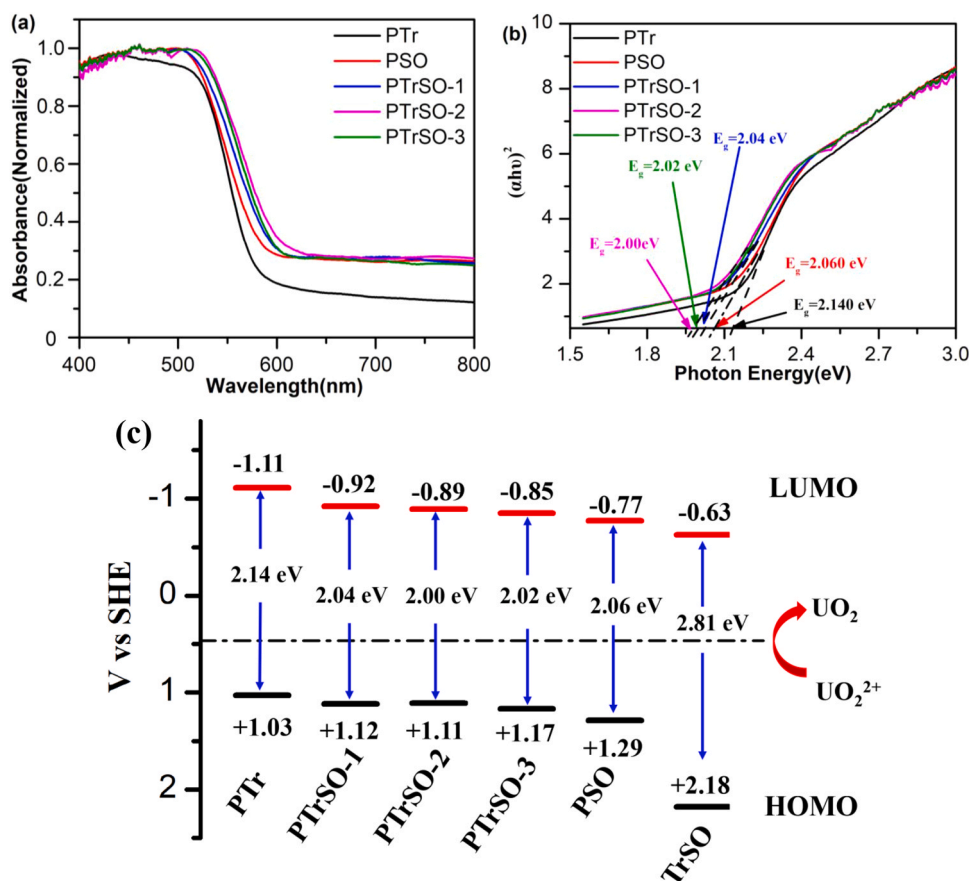


Fig. 4. (a) UV-Vis DRS spectra of CMPs; (b) the bandgaps of CMPs calculated by Tauc-Plot; (c) Energy band diagram of CMPs.

surface and accumulated. Predictably, the PTrSO-2 shows a higher ΔCPD amplitude of 248 mV than PTrSO-1 (206 mV) and PTrSO-3 (225 mV), and much higher than PTr (144 mV), PSO (185 mV) and TrSO (34 mV). The notable increase in ΔCPD peaks of PTrSO-2 certifies the improvement of photogenerated charge transfer along the polymer backbone. Besides, the *i-t* responses (Fig. 5c) of D-A₁-A₂ CMPs with typical on-off cycles are significantly enhanced in comparison with that of D-A copolymer under illumination. The highest photocurrent intensity of PTrSO-2 ($0.62 \mu\text{Acm}^{-2}$) is about 3.07 and 1.72 times that of PTr ($0.30 \mu\text{Acm}^{-2}$) and PSO ($0.36 \mu\text{Acm}^{-2}$), respectively, strongly demonstrating that the photo-generated electrons and holes are efficiently separated by introducing the secondary acceptor unit (sulfone group). Meanwhile, according to the EIS (Fig. 5d), the PTrSO-2 has the smallest arc radius among all CMPs, indicating faster interfacial charge transfer. According to all the results, the construction of D-A₁-A₂ pattern not only promote charge separation but also suppress backward charge recombination, thereby improving photocatalytic activity.

3.6. The density functional theory (DFT) calculations

To investigate the influence of the polymer structure on the intramolecular excited electron-transfer process, the density functional theory (DFT) simulation are carried out with the B3LYP functional and the 6-311 G (d, p) basis set in Gaussian 16 package. As drawn in Fig. 6a, the structures and obtained the molecular orbital diagrams (HOMO and LUMO) of the oligomer models have been optimized. According to the calculation result, the E_g become narrower after constructing D-A₁-A₂ structure, which helps broaden the spectrum. In addition, for PTr and PSO, their HOMOs orbits mostly localizes on the perylene donor part, whereas the LUMOs orbits mainly spread on the electron-withdrawing units (triazine and sulfone units for PTr and PSO, respectively), which

conforms to the characteristics of D-A structure, leading to effective spatial charge separation. Especially, the HOMO orbital of PTrSO-2 still mainly concentrated on perylene, while the LUMO are mainly delocalized over the triazine and sulfone units, which indicates that much higher degree of LUMO-HOMO separation, resulting in more efficient charge separation. Notably, the electrostatic potential distribution (ESP) shows that the sulfone unit in the CMPs is negatively charged, and the other parts are positively charged (Fig. 6b). Therefore, the PTrSO-2 molecule has relatively large dipole (5.62 D) than that of PTr (0.13 D) and PSO (5.38 D). Furthermore, it can be obtained the internal electric field intensity (F_z) of PTrSP-2 is about 1.91 and 1.54 times that of PTr and PSO, respectively. The relevant evidence is provided in the Supporting Information, such as the increased surface photovoltage intensity (Fig. S9a) and the enhanced surface charge density (Fig. S9b). More importantly, the uneven distribution of charges in the polymer backbone will cause a larger molecular dipole moment, thereby inducing the formation of robust enough built-in electric field, which is beneficial for preventing the recombination of back electrons and promoting the separation of electron-hole pairs [55–57].

3.7. Photocatalytic performance and stability

Before light irradiation, the reaction system is placed in the dark for 60 min to achieve the adsorption-desorption equilibrium. Among all, the PTrSO-2 which has a higher content of sulfone groups and the largest specific surface area shows the best dark state adsorption performance with the U(VI) removal rate of 20.9%, mainly as a result of the sulfone group can coordinate well with uranyl ions, and a large BET will provide more coordination sites [46,47]. For comparison, the photocatalytic uranium reduction activity of the obtained CMPs is next systematically investigated in a 100.0 mL 50.0 ppm U(VI) solution at pH = 4.0

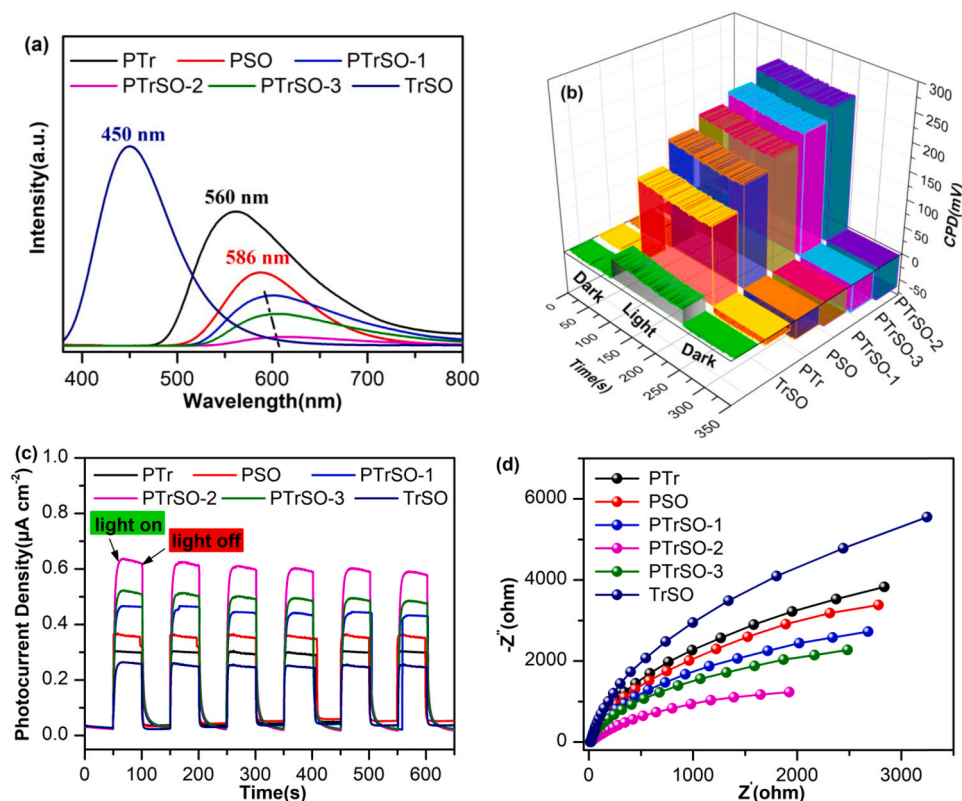


Fig. 5. (a) Photoluminescence spectra of the resulting CMPs under 380 nm excitation; (b) Contact potential difference (CPD) of the resulting CMPs in the dark and under illumination at 500 nm; (c) Transient current responses to on-off cycles of illumination on CMPs membrane electrodes (0 bias) in 0.5 M Na₂SO₄; and (d) EIS Nyquist plots of CMPs at open circuit voltage.

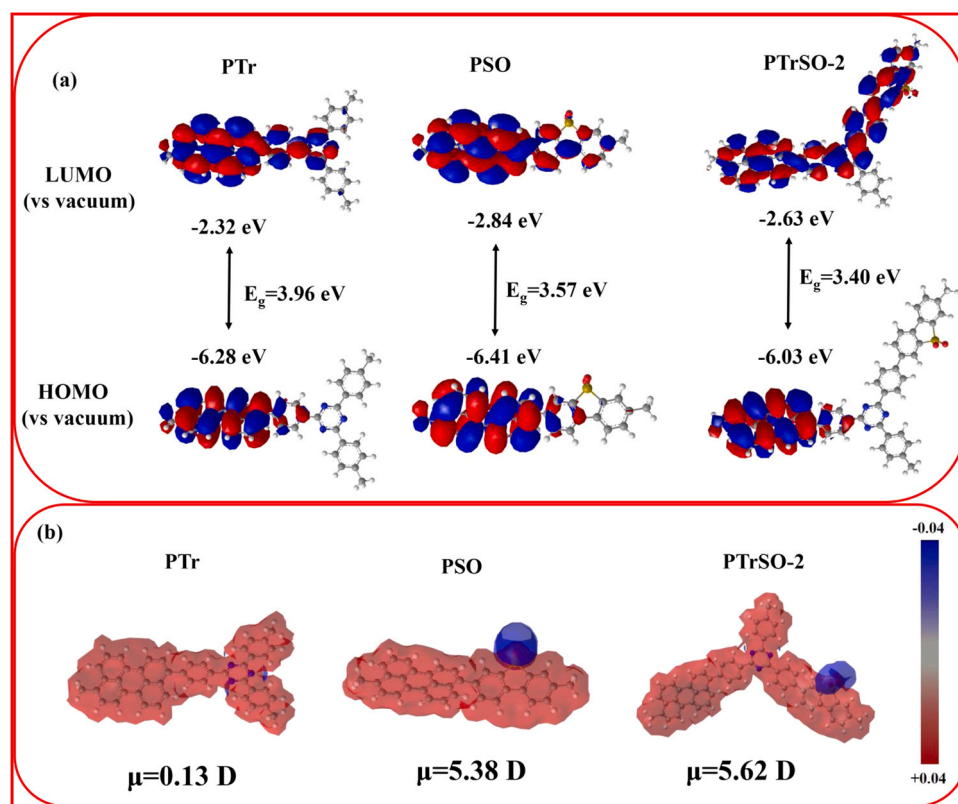


Fig. 6. (a) The HOMO and LUMO orbital distributions of the simplified copolymer fragment from DFT simulation; (b) The electrostatic potential distributions (ESP), and the corresponding dipole moments (the unit of dipole moment: Debye) of PTr, PSO and PTrSO-2.

(Notably: the pH value and initial uranium concentration have been optimized, as shown in Fig. S7) under visible light ($\lambda \geq 400$ nm). As shown in Fig. 6a, no significant change in U(VI) concentration is found under the blank experiment, implying that U(VI) is stable without self-photolysis. Interestingly, the concentration of U(VI) in the reaction system apace decreases under visible light irradiation. After irradiation 120 min, the reduction efficiency (RE) of U(VI) for PTr, PSO, TrSO, PTrSO-1, PTrSO-2 and PTrSO-3 are 85.3%, 95.5%, 71.6%, 98.6%, 99.5% and 98.9%, respectively. The corresponding reduction rates constant (k) at 293.15 K (Fig. 6b) are 0.016, 0.026, 0.011, 0.035, 0.044, 0.038 min^{-1} , respectively, according to the pseudo first-order kinetics model ($\ln(c_0/c_t) = kt$). The results show that the photocatalytic activity of D-A₁-A₂ CMPs are tremendously dependent on the FMR, and an optimal k of 0.044 min^{-1} for photocatalytic reduction of uranium is obtained by PTrSO-2 with a FMR of 0.75: 1: 0.75. Therefore, the enhanced photocatalytic U(VI) reduction activity for PTrSO-2 can be attributed to the synergy of the following three points: (i): broadened visible spectrum response range; (ii) inhibited backward charge recombination and promoted charge separation process; (iii) Increased uranyl ion adsorption sites.

Interestingly, the cycling photocatalytic U(VI) reduction experiment tests show that no significantly activity loss occurs for PTrSO-2 after six cycles (Fig. 7c), demonstrating a high photochemical stability. Subsequently, to evaluate the selectivity of photoreduction U(VI), the influence of interfering ions on photoreduction U(VI) with PTrSO-2 is investigated. As shown in Fig. 7d, the interfering metal ions, including Na^+ , K^+ , VO_2^+ , Mg^{2+} , Sr^{2+} , Zn^{2+} , Co^{2+} , Ni^{2+} , Ca^{2+} , Dy^{3+} , Al^{3+} , Er^{3+} and Yb^{3+} whose concentrations are 50.0 times higher than U(VI) have a slight influence on photoreduction of U(VI), indicating that the PTrSO-2 can effectively and selectively remove U(VI).

3.8. Mechanism analysis

Although it is generally believed that U(VI) is reduced to U(IV) through semiconductor photocatalytic process, the conversion process and the precipitation state of uranium are still controversial and deserve further study. The FT-IR spectra of PTrSO-2 before and after photocatalytic reduction is shown in Fig. 8a. A new characteristic of $\text{O}=\text{U}=\text{O}$ stretch is observed at approximately 940 cm^{-1} in the PTrSO-2 that has been irradiated for 120 min, indicating that uranium-containing species are successfully deposited on the surface of the photocatalyst. Additionally, XPS measurement is carried out to further characterize the valence state of uranium-bearing species. As displayed in O1s spectra (Fig. 8b), a new peak appeared at 530.50 eV is attributed to uranium oxide (O-U) after photocatalytic reaction, and interestingly, its intensity increases with the prolonged exposure time (0–120 min), presumably forming uranium oxide. More importantly, the high-resolution XPS spectra of U4f under dark and after photoreduction are compared in detail. Seen from Fig. 8c, for the PTrSO-2 sample which adsorbs uranium for 60 min in dark, two obvious peaks at 393.21 and 382.37 eV are monitored, which are assigned to the $\text{U}4f_{5/2}$ and $\text{U}4f_{7/2}$ of U(VI), respectively. Especially, after photoreduction, the $\text{U}4f_{5/2}$ (or $\text{U}4f_{7/2}$) signal can be further deconvoluted into two peaks of 393.21 eV (or 382.37 eV) and 391.10 eV (or 380.00 eV), corresponding to U(VI) and the reduced U(IV), respectively. As the photoreaction time is extended from 60 to 120 min, the ratio of U(IV)/U(VI) increases from 0.46 to 0.58. The results indicate that U(VI) is successfully reduced to U(IV) and the two coexist on the surface of the photocatalyst. The before-mentioned results are further championed by the XRD patterns of PTrSO-2 before and after U(VI) photoreduction. As shown in Fig. 8d, it can be seen that for U(VI)-adsorbed PTrSO-2, no new peak is observed, and the peak shape of fresh PTrSO-2 is maintained (Fig. S1a). However, the representative peaks of UO_2 located at $\sim 28.3^\circ$, 32.7° , 46.9° , 55.8° and 78.1° (UO_2 : PDF#41–1422) are detected in the irradiated PTrSO-2, which

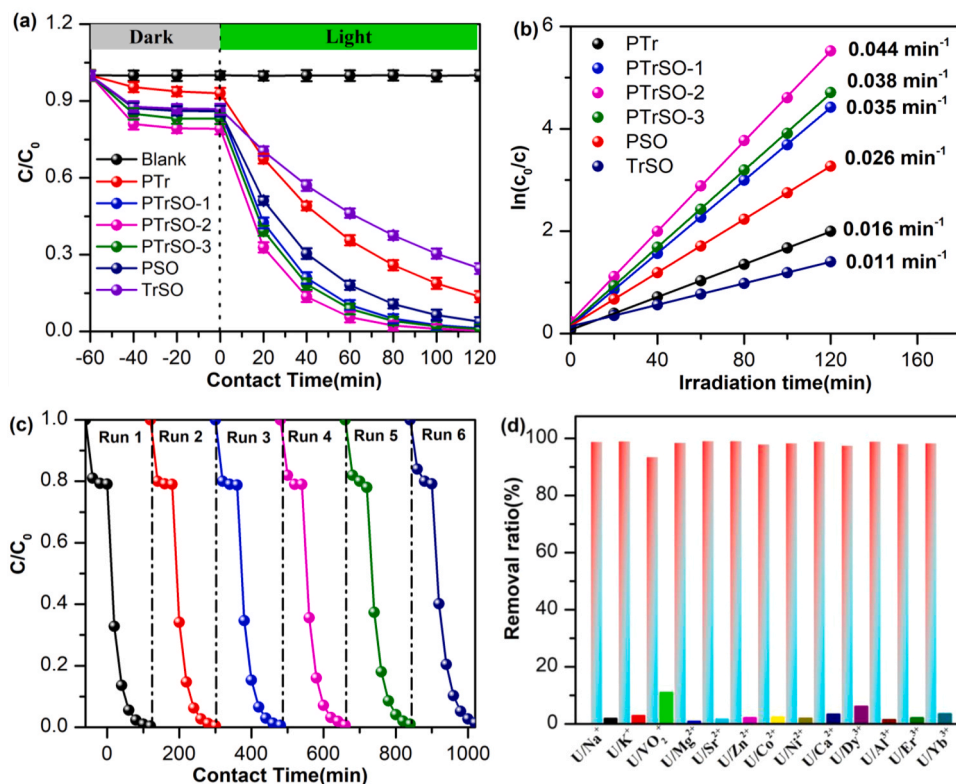


Fig. 7. (a) The variation of UO_2^{2+} concentration vs. illumination time with CMPs as photocatalysts; and (b) The corresponding pseudo-first-order rate constant (k) of UO_2^{2+} reduction; (c) Cycling performance of PTrSO-2; (d) Effects of other competitive ions on photocatalytic removal of uranium for PTrSO-2 (Reaction conditions: 100.0 mL water containing 10.0 mL methanol, 50.0 ppm U(VI), $\text{M}^{n+}/\text{U} = 50.0:1.0$) at pH 4.0, 50.0 mg of PTrSO-2 under visible light).

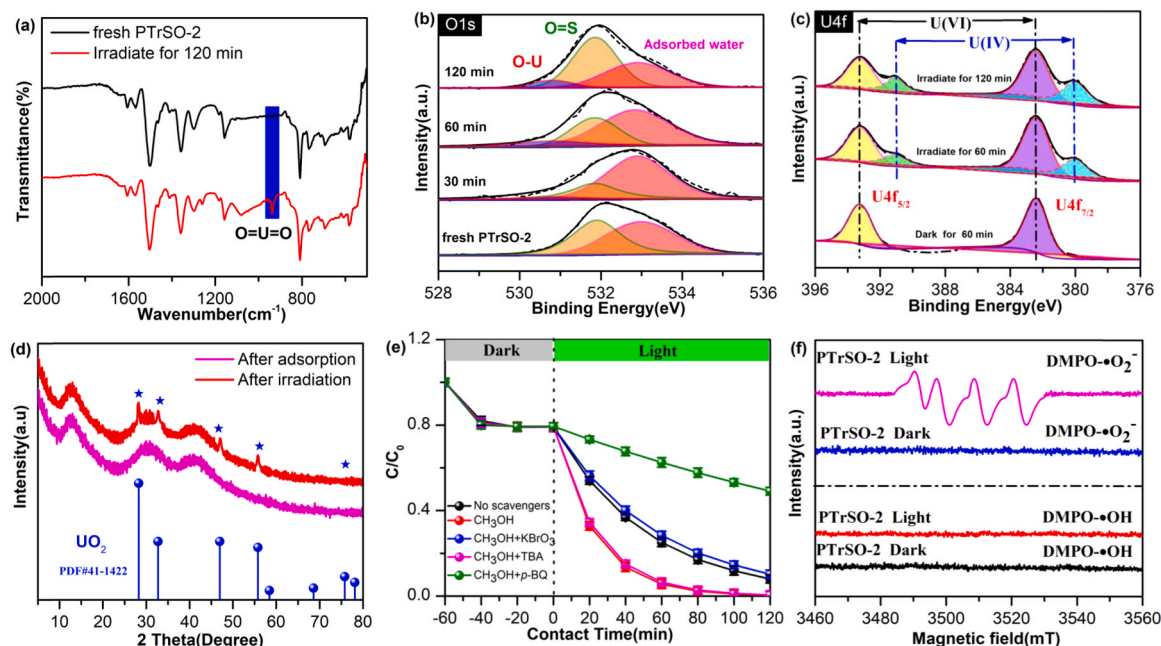


Fig. 8. (a) The FT-IR of PTrSO-2 after photocatalytic reduction of uranium; (b) High-resolution O 1s and (c) U 4f XPS spectra PTrSO-2 after different reaction times, respectively; (d) The XRD of PTrSO-2 after photocatalytic reduction of uranium; (e) Removal of U(VI) by PTrSO-2 with e^- , h^+ , $\bullet O_2^-$ and $\bullet OH$ radical scavenger under visible light irradiation; (f) EPR spectra of $DMPO\cdot\bullet O_2^-$ and $DMPO\cdot\bullet OH$ for PTrSO-2 in dark and light.

further proves that U(VI) is eventually converted to $UO_2(s)$.

Subsequently, to in-depth quest the active species in the entire photoreduction process, the influence of h^+ , e^- , $\bullet OH$ and $\bullet O_2^-$ radicals on removal U(VI) by PTrSO-2 is comparatively presented in Fig. 8e. The CH_3OH , $KBrO_3$, TBA and $p-BQ$ are added as scavengers for h^+ , e^- , $\bullet OH$ radicals and $\bullet O_2^-$ radicals, respectively [58]. Markedly, the existence of TBA has a negligible influence on the photoreduction of U(VI). However, the remarkably enhanced photoreduction of U(VI) in the presence of CH_3OH is attributed to the rapid elimination of h^+ , which enhances the separation of photo-generated e^-/h^+ pairs. Meanwhile, the addition of $p-BQ$ and $KBrO_3$ can significantly inhibit the reduction of U(VI). Therefore, the acquired results indicate that the e^- and $\bullet O_2^-$ are the main reductive species for U(VI) photoreduction. Besides, ESR spin-trapping experiment is deployed to detect the transient radical intermediates ($DMPO\cdot HO\bullet$ and $DMPO\cdot\bullet O_2^-$). As described in Fig. 8f, no $DMPO\cdot HO\bullet$ signals are detected in the dark or under light irradiation. Because the HOMO energy level of PTrSO-2 (+1.11 V) is much higher than the potential position of $OH^-/\bullet OH$ (+1.99 V) and $H_2O/\bullet OH$ (+2.34 V) couples, leading to insufficient driving force to oxidize OH^- or H_2O to $\bullet OH$. Predictably, $DMPO\cdot\bullet O_2^-$ peaks are also not observed in the dark. In contrast, the $DMPO\cdot\bullet O_2^-$ signals are evidently observed under light irradiation, as verified by the four characteristic peaks with identical intensity, indicating the formation of $\bullet O_2^-$ radicals. Because the photogenerated electrons in the LUMO energy level of PTrSO-2 can reduce the dissolved O_2 to $\bullet O_2^-$, which thanks to it has more negative LUMO energy level (-0.89 V) than the reduction potential of the $O_2/\bullet O_2^-$ couple (-0.33 V).

Combining the upon analysis results, a possible photocatalytic uranium reduction mechanism of the D-A₁-A₂ terpolymer is proposed, as shown in Fig. 9. Firstly, the sulfone group in PTrSO-2 undergoes coordinated adsorption with uranyl ions in the dark. After the adsorption-desorption equilibrium is reached, the xenon lamp is turned on immediately. Then, the PTrSO-2 captures photons to generate e^-/h^+ pairs, and driven by robust built-in electric field, the photo-generated electrons are swiftly transferred from the HOMO orbital of perylene donor to the LUMO orbital of dibenzothiophene-S, S-dioxide acceptor along the polymer π -conjugated skeleton. Afterward, some of the excited electrons directly reduce the adsorbed U(VI) to $UO_2(s)$. The other part of the

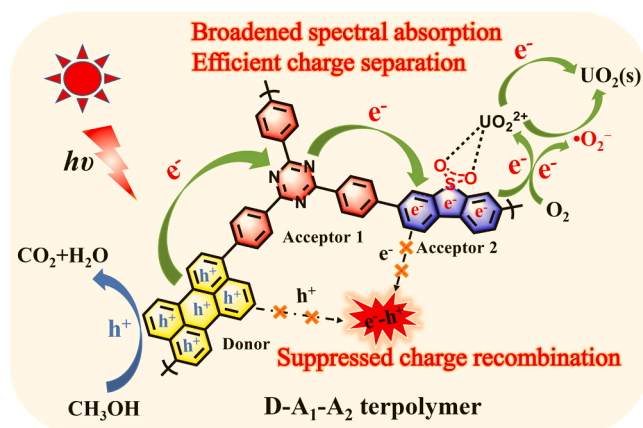


Fig. 9. The proposed photocatalytic mechanism of the D-A₁-A₂ terpolymer photocatalyst.

photo-generated electrons reacts with O_2 to generate $\bullet O_2^-$ radicals, and then the $\bullet O_2^-$ radicals further reduce the adsorbed U(VI) to $UO_2(s)$. Simultaneously, the photo-generated holes oxidize methanol to form carbon dioxide and water, thereby completing the entire photocatalytic process. As a result, such a D-A₁-A₂ system can improve the separation efficiency of electron-hole pairs and inhibit the recombination process of back electrons, thereby significantly enhancing the photocatalytic activity.

4. Conclusions

In summary, a series of D-A₁-A₂ ternary CMPs photocatalysts have been successfully obtained using a statistical copolymerization strategy through adjusting the monomer feed molar ratio (FMR). Interestingly, the photocatalytic U(VI) reduction activity of CMPs is highly dependent on the FMR. As a result, the PTrSO-2 terpolymer which the FMR is set as 0.75: 1.0: 0.75 displays the optimal E_g of 2.00 eV, efficient charge separation and suppressed charge recombination, thus achieving 99.5%

photocatalytic U(VI) reduction efficiency within 120 min visible light irradiation and corresponding reduction rate constant at 293.15 K of 0.044 min^{-1} . In addition, mechanism analysis illustrates that the main active species in the photocatalytic process of U(VI) being reduced to UO_2 are photoelectrons and $\bullet\text{O}_2^-$ radicals. The current research findings are of great significance to the application of conjugated microporous polymer photocatalysts in the efficient treatment of uranium-containing wastewater.

CRedit authorship contribution statement

The manuscript describes original work and is not under consideration by any other journal. **Fengtiao Yu**: Investigation, Methodology, Validation, Funding acquisition, Project administration, Writing – original draft. **Zhiqiang Zhu**: Investigation, Formal analysis, Validation. **Shiping Wang**: Methodology, Investigation. **Jinyu Wang**: Data curation. **Zhenzhen Xu**: Software, Data curation. **Fangru Song**: Funding acquisition, Investigation. **Zhimin Dong**: Writing – review & editing. **Zhibin Zhang**: Conceptualization, Writing – review & editing, Supervision, Project administration, Resources.

Declaration of Competing Interest

The authors declare that they have no known competing financial interests or personal relationships that could have appeared to influence the work reported in this paper.

Acknowledgments

For financial support of this research, we gratefully acknowledge the project supported by Jiangxi Provincial Natural Science Foundation (20202BABL213027); Open-end foundation of Jiangxi Key Laboratory for Mass Spectrometry Instruments (JXMS202013); the National Natural Science Foundation of China (21866004, 22066003, 2210051329) and Research Foundation for Advanced Talents of East China University of Technology (DHBK2019138). Thanks for the monomer of 3,9-dibromoperylene support from Jilin Chinese Academy of Sciences-Yanshen Technology Co., Ltd.

Appendix A. Supporting information

Supplementary data associated with this article can be found in the online version at [doi:10.1016/j.apcatb.2021.120819](https://doi.org/10.1016/j.apcatb.2021.120819).

References

- [1] A. Adamantides, I. Kessides, Nuclear power for sustainable development: current status and future prospects, *Energy Policy* 37 (2009) 5149–5166.
- [2] S. Chu, A. Majumdar, Opportunities and challenges for a sustainable energy future, *Nature* 488 (2012) 294–303.
- [3] K. Mayer, M. Wallenius, K. Lutzenkirchen, J. Horta, A. Nicholl, G. Rasmussen, P. van Belle, Z. Varga, R. Buda, N. Erdmann, J.V. Kratz, N. Trautmann, L.K. Fifield, S.G. Tims, M.B. Frohlich, P. Steier, Uranium from german nuclear power projects of the 1940s—a nuclear forensic investigation, *Angew. Chem. Int. Ed.* 54 (2015) 13452–13456.
- [4] Z.J. Li, Z.W. Huang, W.L. Guo, L. Wang, L.R. Zheng, Z.F. Chai, W.Q. Shi, Enhanced photocatalytic removal of uranium (VI) from aqueous solution by magnetic $\text{TiO}_2/\text{Fe}_3\text{O}_4$ and its graphene composite, *Environ. Sci. Technol.* 51 (2017) 5666–5674.
- [5] W.Z. Zhang, L. Lia, Y.H. Gao, D. Zhang, Graphitic carbon nitride-based materials for photocatalytic reduction of U(VI), *N. J. Chem.* 44 (2020) 19961–19976.
- [6] Y.H. Wang, M. Frutschi, E. Suvorova, V. Phrommavanh, M. Descostes, A.A. Osman, G. Geipel, R. Bernier-Latmani, Mobile uranium(IV)-bearing colloids in a mining-impacted wetland, *Nat. Commun.* 4 (2013) 2942, 2942–2930.
- [7] A.M. Lakaniemi, G.B. Douglas, A.H. Kaksanen, Engineering and kinetic aspects of bacterial uranium reduction for the remediation of uranium contaminated environments, *J. Hazard. Mater.* 371 (2019) 198–212.
- [8] Y. Suzuki, S.D. Kelly, K.M. Kemner, J.F. Banfield, Nanometre-size products of uranium bioreduction, *Nature* 419 (2002) 134. –134.
- [9] R.B. Latmani, H. Veeramani, E.D. Vecchia, P. Junier, J.S. Pacheco, E.I. Suvorova, J. O. Sharp, N.S. Wigginton, J.R. Bargar, Non-uraninite products of microbial U(VI) reduction, *Environ. Sci. Technol.* 44 (2010) 9456–9462.
- [10] Z.Z. Pan, B. Bártová, T. LaGrange, S.M. Butorin, N.C. Hyatt, M.C. Stennett, K. O. Kvashnina, R.B. Latmani, Nanoscale mechanism of UO_2 formation through uranium reduction by magnetite, *Nat. Commun.* 11 (2020) 4001–40012.
- [11] L. Wang, H. Song, L.Y. Yuan, Z.J. Li, Y.J. Zhang, J.K. Gibson, L.R. Zheng, Z.F. Chai, W.Q. Shi, Efficient U(VI) reduction and sequestration by Ti_2CT_x MXene, *Environ. Sci. Technol.* 52 (2018) 10748–10756.
- [12] P. Li, J.J. Wang, Y. Wang, J.J. Liang, B.H. He, D.Q. Pan, Q.H. Fan, X.K. Wang, Photoconversion of U(VI) by TiO_2 : An efficient strategy for seawater uranium extraction, *Chem. Eng. J.* 365 (2019) 231–241.
- [13] F.T. Yu, Z.W. Yu, Z.Z. Xu, J.B. Xiong, Q.W. Fan, X.F. Feng, Y. Tao, J.L. Hua, F. Luo, Heteroatom engineering of polymeric carbon nitride heterojunctions for boosting photocatalytic reduction of hexavalent uranium, *Mol. Syst. Des. Eng.* 5 (2020) 882–889.
- [14] E. Selli, V. Eliet, M.R. Spini, G. Bidoglio, Effects of humic acids on the photoinduced reduction of U(VI) in the presence of semiconducting TiO_2 particles, *Environ. Sci. Technol.* 34 (2000) 3742–3748.
- [15] Y.K. Kim, S. Lee, J. Ryu, H. Park, Solar conversion of seawater uranium (VI) using TiO_2 electrodes, *Appl. Catal. B: Environ.* 163 (2015) 584–590.
- [16] V.N. Salomone, J.M. Meichtry, M.I. Litter, Heterogeneous photocatalytic removal of U(VI) in the presence of formic acid: U(III) formation, *Chem. Eng. J.* 270 (2015) 28–35.
- [17] Z.J. Li, Z.W. Huang, W.L. Guo, L. Wang, L.R. Zheng, Z.F. Chai, W.Q. Shi, Enhanced photocatalytic removal of Uranium (VI) from aqueous solution by magnetic $\text{TiO}_2/\text{Fe}_3\text{O}_4$ and its graphene composite, *Environ. Sci. Technol.* 51 (2017) 5666–5674.
- [18] H. Deng, Z.J. Li, L. Wang, L.Y. Yuan, J.H. Lan, Z.Y. Chang, Z.F. Chai, W.Q. Shi, Nanolayered Ti_3C_2 and SrTiO_3 composites for photocatalytic reduction and removal of uranium (VI), *ACS Appl. Nano Mater.* 2 (2019) 2283–2294.
- [19] P.L. Liang, L.Y. Yuan, K. Du, L. Wang, Z.J. Li, H. Deng, X.C. Wang, S.Z. Luo, W. Q. Shi, Photocatalytic reduction of uranium (VI) under visible light with 2D/1D $\text{Ti}_3\text{C}_2/\text{CdS}$, *Chem. Eng. J.* 420 (2021) 129831–129840.
- [20] X.L. Tong, S. Wang, J. Zuo, Y.C. Ge, Q. Gao, S.J. Liu, J.H. Ding, F. Liu, J.Q. Luo, J. B. Xiong, Two 2D uranyl coordination complexes showing effective photocatalytic degradation of Rhodamine B and mechanism study, *Chin. Chem. Lett.* 32 (2021) 604–608.
- [21] J.S.M. Lee, A.I. Cooper, Advances in conjugated microporous polymers, *Chem. Rev.* 120 (2020) 2171–2214.
- [22] X.C. Wang, K. Maeda, A. Thomas, K. Takanabe, G. Xin, J.M. Carlsson, K. Domen, M. Antonietti, A metal-free polymeric photocatalyst for hydrogen production from water under visible light, *Nat. Mater.* 8 (2009) 76–80.
- [23] H.H. Wang, H. Guo, N. Zhang, Z.S. Chen, B.W. Hu, X.K. Wang, Enhanced photoreduction of U(VI) on C_3N_4 by Cr (VI) and bisphenol A: ESR, XPS, and EXAFS investigation, *Environ. Sci. Technol.* 53 (2019) 6454–6461.
- [24] Z.S. Wu, X.F. He, Y.T. Xue, X. Yang, Y.F. Li, Q.B. Li, B. Yu, Cyclodextrins grafted $\text{MoS}_2/\text{g-C}_3\text{N}_4$ as high-performance photocatalysts for the removal of glyphosate and Cr (VI) from simulated agricultural runoff, *Chem. Eng. J.* 399 (2020) 125747–125757.
- [25] C. Liu, Z.M. Dong, C.H. Yu, J.Y. Gong, Y.Q. Wang, Z.B. Zhang, Y.H. Liu, Study on photocatalytic performance of hexagonal $\text{SnS}_2/\text{g-C}_3\text{N}_4$ nanosheets and its application to reduce U(VI) in sunlight, *Appl. Surf. Sci.* 537 (2021) 147754–147764.
- [26] P. Li, Y. Wang, J.J. Wang, L. Dong, W.T. Zhang, Z.H. Lu, J.J. Liang, D.Q. Pan, Q. H. Fan, Carboxyl groups on $\text{g-C}_3\text{N}_4$ for boosting the photocatalytic U(VI) reduction in the presence of carbonates, *Chem. Eng. J.* 414 (2021) 128810–128818.
- [27] R.S. Sprick, J.X. Jiang, B. Bonillo, S.J. Ren, T. Ratvijitvech, P. Guiglion, M. A. Zwiñenburg, D.J. Adams, A.I. Cooper, Tunable organic photocatalysts for visible-light-driven hydrogen evolution, *J. Am. Chem. Soc.* 137 (2015) 3265–3270.
- [28] A.A. Lan, M. Wu, Z.P. Fang, X. Chi, X. Chen, Y.F. Zhang, X.C. Wang, A fully coplanar donor–acceptor polymeric semiconductor with promoted charge separation kinetics for photochemistry, *Angew. Chem. Int. Ed.* 60 (2021) 16355–16359.
- [29] C.H. Dai, L.X. Zhong, X.Z. Gong, L. Zeng, C. Xue, S.Z. Li, B. Liu, Triphenylamine based conjugated microporous polymers for selective photoreduction of CO_2 to CO under visible light, *Green. Chem.* 21 (2019) 6606–6610.
- [30] Y.O. Wang, A. Vogel, M. Sachs, R.S. Sprick, L. Wilbraham, S.A. Moniz, R. Godin, M. A. Zwiñenburg, J.R. Durrant, A.I. Cooper, J.W. Tang, Current understanding and challenges of solar-driven hydrogen generation using polymeric photocatalysts, *Nat. Energy* 4 (2019) 746–760.
- [31] F. Lan, Q. Wang, H. Chen, Y. Chen, Y.Y. Zhang, B.W. Huang, H.B. Liu, J. Liu, R. Li, Preparation of hydrophilic conjugated microporous polymers for efficient visible light-driven nicotinamide adenine dinucleotide regeneration and photobiocatalytic formaldehyde reduction, *ACS Catal.* 10 (2020) 12976–12986.
- [32] L.P. Guo, X.P. Wang, Z. Zhan, Y.L. Zhao, L.J. Chen, T. Liu, B.E. Tan, S.B. Jin, Crystallization of covalent triazine frameworks via a heterogeneous nucleation approach for efficient photocatalytic applications, *Chem. Mater.* 33 (2021) 1994–2003.
- [33] L.P. Guo, X.P. Wang, Z. Zhan, Y.L. Zhao, L.J. Chen, T. Liu, B.E. Tan, S.B. Jin, Crystallization of covalent triazine frameworks via a heterogeneous nucleation approach for efficient photocatalytic applications, *Chem. Mater.* 33 (2021) 1994–2003.
- [34] W.R. Cui, F.F. Li, R.H. Xu, C.R. Zhang, X.R. Chen, R.H. Yan, R.P. Liang, J.D. Qiu, Regenerable covalent organic frameworks for photo-enhanced uranium adsorption from seawater, *Angew. Chem. Int. Ed.* 59 (2020) 17684–17690.
- [35] W.R. Cui, C.R. Zhang, R.H. Xu, X.R. Chen, W. Jiang, Y.J. Li, R.P. Liang, L. Zhang, J. D. Qiu, Rational design of covalent organic frameworks as a groundbreaking uranium capture platform through three synergistic mechanisms, *Appl. Catal. B: Environ.* 294 (2021) 120250–120260.

- [36] G.S. Zhu, Reaction: goal-oriented PAF design for uranium extraction from seawater, *Chem* 7 (2021) 277–278.
- [37] Y.Y. Tian, G.S. Zhu, Porous aromatic frameworks (PAFs), *Chem. Rev.* 120 (2020) 8934–8986.
- [38] Y. Yuan, Y.J. Yang, G.S. Zhu, Molecularly imprinted porous aromatic frameworks for molecular recognition, *ACS Cent. Sci.* 6 (2020) 1082–1094.
- [39] M.H. Elsayed, J. Jayakumar, M. Abdellah, T.H. Mansoure, K.B. Zheng, A.M. Elewa, C.L. Chang, L.Y. Ting, W.C. Lin, H.H. Yu, W.H. Wang, C.C. Chung, H.H. Chou, Visible-light-driven hydrogen evolution using nitrogen-doped carbon quantum dot-implanted polymer dots as metal-free photocatalysts, *Appl. Catal. B: Environ.* 283 (2021) 119659–119671.
- [40] P.J. Tseng, C.L. Chang, Y.H. Chan, L.Y. Ting, P.Y. Chen, C.H. Liao, M.L. Tsai, H. H. Chou, Design and synthesis of cycloplatinated polymer dots as photocatalysts for visible-light-driven hydrogen evolution, *ACS Catal.* 8 (2018) 7766–7772.
- [41] F.T. Yu, Z.Q. Wang, S.C. Zhang, W.J. Wu, H.N. Ye, H.R. Ding, X.Q. Gong, J.L. Hua, Construction of polymeric carbon nitride and dibenzothiophene dioxide-based intramolecular donor–acceptor conjugated copolymers for photocatalytic H₂ evolution, *Nanoscale Adv.* 3 (2021) 1699–1707.
- [42] Z.J. Wang, X.Y. Yang, T.J. Yang, Y.B. Zhao, F. Wang, Y. Chen, J.H. Zeng, C. Yan, F. Huang, J.X. Jiang, Dibenzothiophene dioxide based conjugated microporous polymers for visible-light-driven hydrogen production, *ACS Catal.* 8 (2018) 8590–8596.
- [43] F.T. Yu, Z.Q. Wang, S.C. Zhang, H.N. Ye, K.Y. Kong, X.Q. Gong, J.L. Hua, H. Tian, Molecular engineering of Donor-Acceptor conjugated polymer/g-C₃N₄ heterostructures for significantly enhanced hydrogen evolution under visible-light irradiation, *Adv. Funct. Mater.* 28 (2018) 1804512–1804524.
- [44] Z.A. Lan, W. Ren, X. Chen, Y.F. Zhang, X.C. Wang, Conjugated donor-acceptor polymer photocatalysts with electron-output “tentacles” for efficient hydrogen evolution, *Appl. Catal. B: Environ.* 245 (2019) 596–603.
- [45] J.L. Wang, G.C. Ouyang, Y. Wang, X.L. Qiao, W.S. Li, H.X. Li, 1,3,5-Triazine and dibenzo[b,d]thiophene sulfone based conjugated porous polymers for highly efficient photocatalytic hydrogen evolution, *Chem. Commun.* 56 (2020) 1601–1604.
- [46] F.T. Yu, Z.Q. Zhu, S.P. Wang, Y.K. Peng, Z.Z. Xu, Y. Tao, J.B. Xiong, Q.W. Fan, F. Luo, Tunable perylene-based donor-acceptor conjugated microporous polymer to significantly enhance photocatalytic uranium extraction from seawater, *Chem. Eng. J.* 412 (2021) 127558–127569.
- [47] F.T. Yu, F.R. Song, R.Z. Wang, M. Xu, F. Luo, Sulfonated perylene-based conjugated microporous polymer as a high-performance adsorbent for photo-enhanced uranium extraction from seawater, *Polym. Chem.* 12 (2021) 867–875.
- [48] A.J. Cowan, J.R. Durrant, Long-lived charge separated states in nanostructured semiconductor photoelectrodes for the production of solar fuels, *Chem. Soc. Rev.* 42 (2013) 2281–2293.
- [49] S. Berardi, S. Drouet, L. Franca's, C.G. Surinãch, M. Guttentag, C. Richmond, T. Stoll, A. Llobet, Molecular artificial photosynthesis, *Chem. Soc. Rev.* 43 (2014) 7501–7519.
- [50] Y.S. Kochergin, D. Schwarz, A. Acharjya, A. Ichangi, R. Kulkarni, P. Eliášová, J. Vacek, J. Schmidt, A. Thomas, M.J. Bojdys, Exploring the “Goldilocks Zone” of semiconducting polymer photocatalysts by donor–acceptor interactions, *Angew. Chem. Int. Ed.* 57 (2018) 1–6.
- [51] T. Yanai, D. Tew, N. Handy, A new hybrid exchange–correlation functional using the Coulomb-attenuating method (CAM-B3LYP), *Chem. Phys. Lett.* 393 (2004) 51–57.
- [52] C. Less, W. Yang, R.G. Parr, Development of the Colle-Salvetti correlation-energy formula into a functional of the electron density, *Phys. Rev. B* 37 (1988) 785–789.
- [53] C. Shu, C.Z. Han, X.Y. Yang, C. Zhang, Y. Chen, S.J. Ren, F. Wang, F. Huang, J. X. Jiang, Boosting the photocatalytic hydrogen evolution activity for D–π–A conjugated microporous polymers by statistical copolymerization, *Adv. Mater.* 33 (2021) 2008498–2008507.
- [54] L.P. Guo, Y.L. Niu, S. Razzaque, B.E. Tan, S.B. Jin, Design of D–A₁–A₂ covalent triazine frameworks via copolymerization for photocatalytic hydrogen evolution, *ACS Catal.* 9 (2019) 9438–9445.
- [55] Z.J. Zhang, X.J. Chen, H.J. Zhang, W.X. Liu, W. Zhu, Y.F. Zhu, A highly crystalline perylene imide polymer with the robust built-in electric field for efficient photocatalytic water oxidation, *Adv. Mater.* 32 (2020) 1907746–1907751.
- [56] Z.J. Zhang, Y.F. Zhu, X.J. Chen, H.J. Zhang, J. Wang, A full-spectrum metal-free porphyrin supramolecular photocatalyst for dual functions of highly efficient hydrogen and oxygen evolution, *Adv. Mater.* 31 (2019) 1806626–1806631.
- [57] X.J. Chen, J. Wang, Y.Q. Chai, Z.J. Zhang, Y.F. Zhu, Efficient photocatalytic overall water splitting induced by the giant internal electric field of a g-C₃N₄/rGO/PDIP Z-Scheme heterojunction, *Adv. Mater.* 33 (2021) 2007479–2007484.
- [58] Z.R. Dai, Y. Zhen, Y.S. Sun, L. Li, D.X. Ding, ZnFe₂O₄/g-C₃N₄ S-scheme photocatalyst with enhanced adsorption and photocatalytic activity for uranium (VI) removal, *Chem. Eng. J.* 415 (2021) 129002–129011.